

Article

The Effect of Asynchronous Grouting Pressure Distribution on Ultra-Large-Diameter Shield Tunnel Segmental Response

Chen Wang¹, Ming Song^{2,3}, Min Zhu^{1,*}, Xiangsheng Chen¹  and Xiaohua Bao¹ 

¹ School of Civil and Transportation Engineering, Shenzhen University, Shenzhen 518061, China; wangchen2021@email.szu.edu.cn (C.W.)

² China Communications Construction Company Second Highway Consultant Co., Ltd., Wuhan 430056, China

³ Research and Development Center on Tunnel and Underground Space Technology, China Communications Construction Company, Wuhan 430056, China

* Correspondence: zhuminfnf@szu.edu.cn

Abstract: The complex distribution of synchronous grouting pressure results in excessive tunnel deformation and various structural diseases, especially for ultra-large-diameter shield tunnels. In this study, to reduce the risk of tunnel failure, a three-dimensional refined finite element model was established for the Wuhan Lianghu highway tunnel project, taking into account the non-uniform distribution of synchronous grouting pressure. This study focuses on investigating the development patterns of internal forces, deformations, and damages in segment structures under varying grouting pressure ratios. The results indicate that the primary failure mode of a segment is tensile failure occurring at the outer edge of the arch. Moreover, an increased ratio of grouting pressure between the arch bottom and top leads to a higher positive bending moment value and greater tensile damage at the arch waist. The tunnel ring gradually exhibits distinct “horizontal duck egg” shape deformation. When the grouting pressure ratio is 2.8, there is a risk of tensile cracking at the outer edge of the arch waist. At this time, the segment convergence deformation is 39.71 mm, and the overall floating amount reaches 43.12 mm. This research offers engineering reference for the prediction of internal forces and deformations in ultra-large-diameter shield tunnels during grouting construction, thereby facilitating their application in the development of resilient cities.

Keywords: numerical model; ultra-large-diameter shield tunnel; synchronous grouting; grouting pressure ratio; tunnel convergence; tensile damage

MSC: 74S05; 65Z05; 00A06



Citation: Wang, C.; Song, M.; Zhu, M.; Chen, X.; Bao, X. The Effect of Asynchronous Grouting Pressure Distribution on Ultra-Large-Diameter Shield Tunnel Segmental Response.

Mathematics **2023**, *11*, 4502. <https://doi.org/10.3390/math11214502>

Academic Editor: Andrey Jivkov

Received: 9 October 2023

Revised: 25 October 2023

Accepted: 30 October 2023

Published: 31 October 2023



Copyright: © 2023 by the authors. Licensee MDPI, Basel, Switzerland. This article is an open access article distributed under the terms and conditions of the Creative Commons Attribution (CC BY) license (<https://creativecommons.org/licenses/by/4.0/>).

1. Introduction

With the continuous advancement of tunnel construction equipment and technology, ultra-large-diameter shield tunnels have become an influential development trend [1–3]. During the shield tunneling process, it is necessary to fill the gap between the segment ring and the surrounding strata by synchronous grouting. When the synchronous grout pressure is not properly controlled, large upheavals may occur, especially for ultra-large-diameter shield tunnels, which can cause serious structural diseases, including segment cracks, misalignment, damage, and leakage [4–7].

The pressure profile of synchronous grouting has been extensively studied by scholars around the world. Regarding the theoretical model, in order to calculate the grout filling pressure and diffusion distance, Li et al. [8] developed a compound diffusion model on a semi-elliptic surface without predetermined flow channels. Ye et al. [9] developed a hemispherical diffusion model that takes into account the percolation effect of synchronous grouting in shield tunnel construction. In addition to theoretical models that reveal the distribution of synchronous grouting pressure along the segment rings [10], physical model testing, as an intuitive and direct experimental method, also plays a crucial role

in scientific research. In practical engineering, maximum synchronous grouting pressure can be solved by testing the control of tunnel displacement and deformation [11,12]. The distribution and long-term evolution of grouting pressure can also be obtained through on-site monitoring [13]. For example, Hashimoto et al. [14] outlined the development of tunnel grouting pressure during construction and long-term grouting, and the resulting lining bending moments. Talmon et al. [15] analyzed the grouting consolidation and formation process of the Groene Hart tunnel under field conditions. More importantly, the theoretical models can be verified by the physical model tests. Assuming that the grouting pressure varies as a power function with time, Zhao et al. [16] proposed a simulation framework to explain the observations in the model tests. Based on the existing theoretical models and physical model tests, most of the research on synchronous grouting pressure has been focused on conventional subway shield tunnels, while less work has been done on the synchronous grouting pressure distribution patterns in ultra-large-diameter shield tunnels.

In addition, with the rapid development of computers, the effect of synchronous grouting on the stress and deformation of the lining structure has also been studied through numerical simulations. Lavasan et al. [17,18] considered three different variants of simulated synchronous grouting to study the impact of synchronous grouting on the tunnel excavation process. In variant I, the slurry is regarded as a distributed load applied on the soil. Due to its simplicity and computational ease, this numerical simulation method is currently used in most studies [19]. On this basis, numerous scholars have also studied the influence of grouting pressure changes on the deformation and mechanical properties of foundation pits and tunnels [20,21]. With the increasing size of modern tunnels, research on large-diameter tunnels and even ultra-large-diameter tunnels is becoming more and more significant [22]. For an ultra-large-diameter shield tunnel, the grout pressure difference between the vaults is larger due to the influence of the grout self-weight during the synchronous grouting process, and the segment is divided into multiple blocks with complex structures. Therefore, the stress and deformation patterns of the lining structure are also complex, but there are few relevant studies.

In this study, to investigate the mechanical response of ultra-large-diameter tunnels under asynchronous grouting pressure more clearly, a three-dimensional refined finite element model was established based on the engineering case of the Wuhan Lianghu highway tunnel. The deformation and damage properties of the tunnel segment were studied for different grout pressure ratios, and the weak position of the segment was determined. The results provide theoretical support for the scientific control of the synchronous grouting pressure in ultra-large-diameter tunnels.

2. Engineering Background

2.1. Project Overview

The Wuhan Lianghu highway tunnel is the largest double-layer, ultra-large-diameter shield tunnel in China. The project is situated in the southern region of Wuhan City, which serves as the capital of Hubei Province in China. Its primary objective is to facilitate direct connectivity between the northern and southern sectors of Wuchang District, thereby enhancing the overall road network within this district. The Lianghu Tunnel project spans a total distance of 19.25 km, encompassing both the East Lake and South Lake sections. The total length of the shielding section is 13.3 km. The diameter of the shield machine is 16.2 m, the outer diameter of the segment ring is 15.5 m, and the thickness of the segment is 0.65 m. The surrounding environment of the tunnel is complex, passing numerous existing roads, Metro lines 4 and 8, and multiple underground pipelines. As shown in Figure 1, the section of the Lianghu tunnel under the Wuxian railway was chosen for analysis in this study. The radius of curvature of the tunnel is 700 m, the longitudinal slope is 0.5%, and the buried depth is 16.5 m (1.02 D). The angle between Lianghu tunnel and Wuxian railway is about 65°.

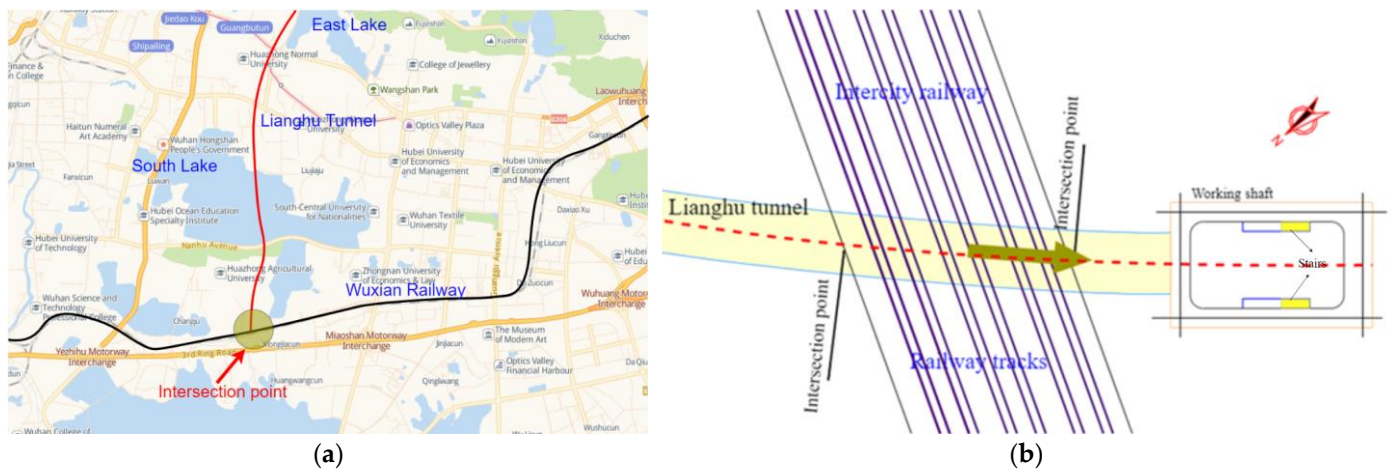


Figure 1. Lianghu Tunnel and Wuxian Intercity Railway. (a) Location map and (b) Intersection plan.

2.2. Geological Conditions

Figure 2 shows the longitudinal geological profile. The overlying soil layer of the shield tunnel is a sequence of plain fill, gravel, mudstone, and mudstone greywacke. The average thickness of the plain fill and gravel soil is about 0.5 m and 4.5 m, respectively. The inference of the formation beneath the intercity railway is based on the geological borehole adjacent to the railway, as drilling is not feasible within the railway area. In accordance with the geotechnical engineering geological investigation report, Table 1 presents the corresponding geological attributes.

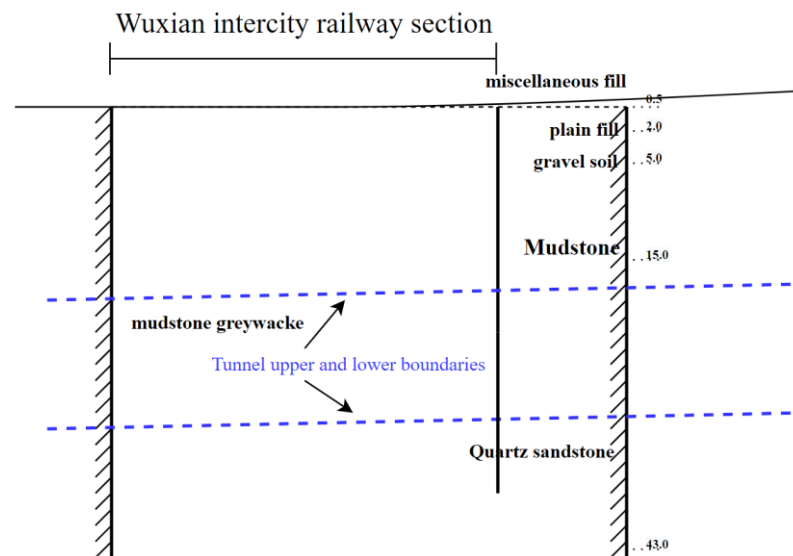


Figure 2. Geological profile.

Table 1. Physical and mechanical parameters of the stratum.

Stratum	γ (kg/m ³)	$E_{S0.1-0.2}$ (MPa)	ν	φ (°)	c (kPa)
Plain fill	19.2	3.8	0.40	13	10
Gravel soil	19.5	25	0.29	27	10
Mudstone	23.5	60	0.36	28	150
Mudstone greywacke	25.6	90	0.35	29	200

3. Establishment of the Finite Element Model

3.1. Overview

The numerical model of the shield tunnel segment is shown in Figure 3. The segmented ring has an outer diameter of 1550 mm, a thickness of 650 mm, and a width of 2000 mm. As shown in Figure 3a, the lining ring is composed of 10 prefabricated reinforced concrete segments, including 1 capping block (F), 2 adjacent blocks (L1 and L2) and 7 standard blocks (B1, B2, B3, B4, B5, B6, and B7). The segments are connected by 30 oblique bolts with a diameter of 36 mm and a length of 740 mm, which is shown in Figure 3b. The mesh of both the segments and the bolts adopts hexahedral grids, and the element type is eight-node linear element C3D8R. The finite element model of the whole segment ring is shown in Figure 4.

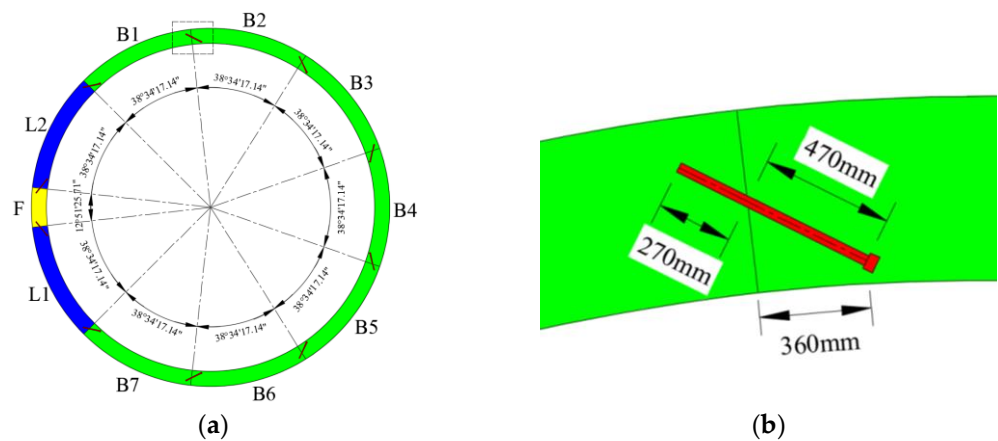


Figure 3. Schematic diagram of (a) segment block and (b) bolt structure.

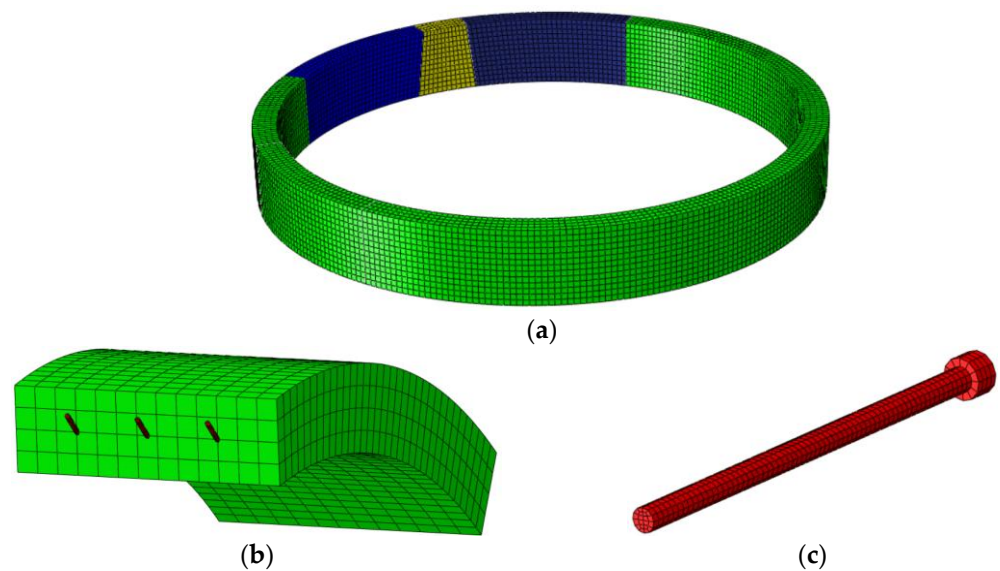


Figure 4. (a) Integral ring, (b) segment, and (c) bolt.

3.2. Material Parameters

The strength grade of precast concrete used in the segment is C60, and the parameters of its compression and tension damage characteristics are determined by the “Code for Design of Concrete Structures” (GB50010-2010) [23]. Table 2 shows the parameters of the plastic damage model for C60 concrete. The bolts adopt the elastic–plastic constitutive model, with elastic modulus $E = 200$ GPa, Poisson’s ratio $\mu = 0.3$, yield strength $f_y = 640$ MPa,

and ultimate strength $f = 800$ MPa. When the bolt stress reaches the yield stress, the modulus of elasticity decreases to 1/100 of its previous value.

Table 2. C60 concrete plastic damage model parameters.

Parameter	Value
ρ (kg/m ³)	2500
E (GPa)	36
ν	0.2
ψ (°)	40
ϵ	0.1
f_{b0}/f_{c0}	1.16
K_c	0.66667
μ	0.0005
σ_{cf} (MPa)	38.5
ϵ_{c0}	0.00177
σ_{tf} (MPa)	2.85
ϵ_{t0}	0.00011

3.3. Boundary Conditions and Interactions

The model of the load-structure method is developed for the calculations. As shown in Figure 5, the interaction between the soil and the segmented lining is simulated by ground springs arranged around the segmented ring, which can accurately reflect the resistance generated by the stratum [24]. The ground springs consist of one normal spring and two tangential springs (shown in Figure 6). The normal spring is only under compression but not tension, and the parameters can be obtained by multiplying the bed coefficient of the stratum by the unit area. In the calculated example, the bed coefficient is 5 kN/m³. According to the results of Koyama [25] and Wang [26], the parameters of a tangential spring are 1/3 of those of a normal spring.

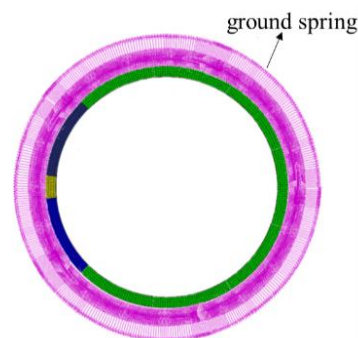


Figure 5. Boundary conditions.

Figure 7 shows the contact setting method for segment–segment and segment–bolt. The contacts between adjacent segments are modeled by surface-to-surface contacts. Finite slip tracking and face-to-face discretization methods were used in the analysis. Finite slip tracking is the most general tracking method, allowing for arbitrary relatively separated, sliding, and rotating contact surfaces, and is suitable for relatively large slides. Face-to-face discretization can better solve the problem of primary surface nodes penetrating the secondary surface. The tangential mechanical properties and normal mechanical properties of the contact obey the penalty function and rough contact, respectively, and the friction coefficient is 0.5 [27]. The accuracy of the calculation results of the local structure in the model is directly influenced by the level of refinement in this part during numerical simulation calculations. However, the focus of this study is not to study the specific analysis of the bolt joint, so the contact between the segment and the bolt is simulated by embedding.

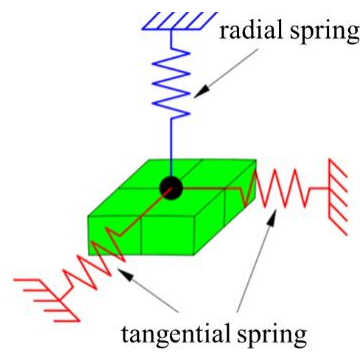


Figure 6. Ground springs schematic.

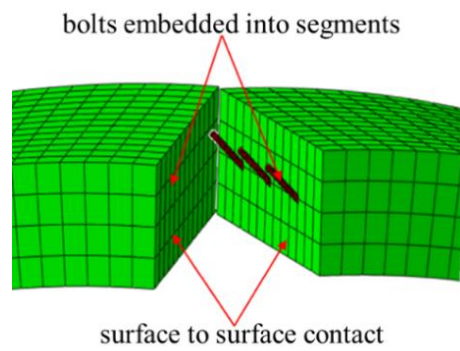


Figure 7. Schematic diagram of the seam contact simulation setup.

3.4. Grouting Pressure Distribution

The grouting pressure is applied to the tunnel segment as an isotropic hydrostatic pressure, and its magnitude and distribution have a strong influence on the results of the calculation of the overall deformation of the tunnel segment. Using the non-uniform grouting pressure distribution model that considers the self-weight of the grout, the upper half ring adopts uniform pressure distribution, and the lower half ring increases linearly according to the pressure difference between the top and the bottom of the tunnel (Figure 8), which is consistent with the distribution form of grouting pressure proposed in the literature [17,28]. The pressure at the vault was determined from the pressure at the excavation face, and the static earth pressure at the tunnel axis was 421.66 kPa. Therefore, the grouting pressure of the vault is selected as 420 kPa, and the pressure ratio of the vault bottom and the vault is set to 1.0, 2.0, 2.4, 2.6, and 2.8, for a total of five groups (respectively, working conditions ① to ⑤).

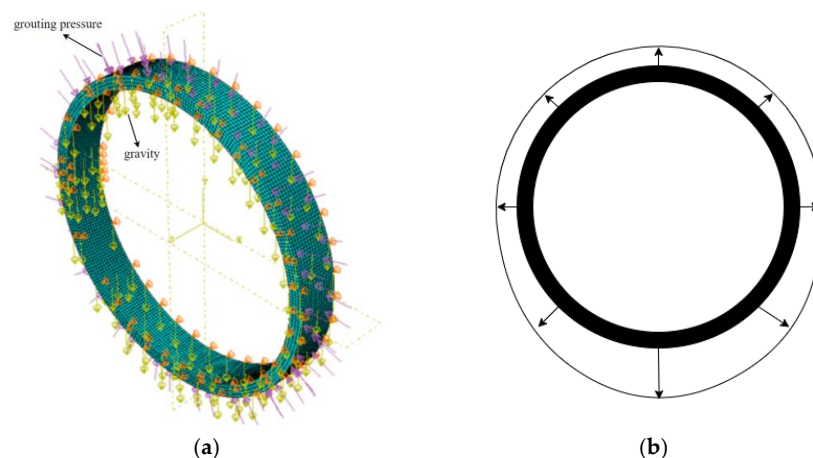


Figure 8. (a) Schematic diagram of pipe ring stress; (b) grouting pressure distribution pattern.

4. Calculation Results Analysis

4.1. Damage Evolution of Tunnel Segment

Figures 9 and 10, respectively, show the tensile and compressive damage cloud diagrams of the shield tunnel concrete segments for different grouting pressure distribution forms, where the deformation display is enlarged by 20 times. As can be seen from Figure 9, the concrete is in a fully elastic state until the tunnel segment grouting pressure ratio is 1:2.4. As the segmental arch bottom grouting pressure increases, the concrete tensile damage factor gradually increases and is mostly distributed at the arch waist edge position. And when the grouting pressure ratio of the segment vault bottom and the vault reaches 1:2.8, the tensile damage factor of the concrete reaches 0.87 and there is a risk of cracking. Since the compressive strength of concrete is much greater than the tensile strength, the compressive damage of concrete tunnel segments under different grouting pressure distribution forms is significantly smaller than the tensile damage.

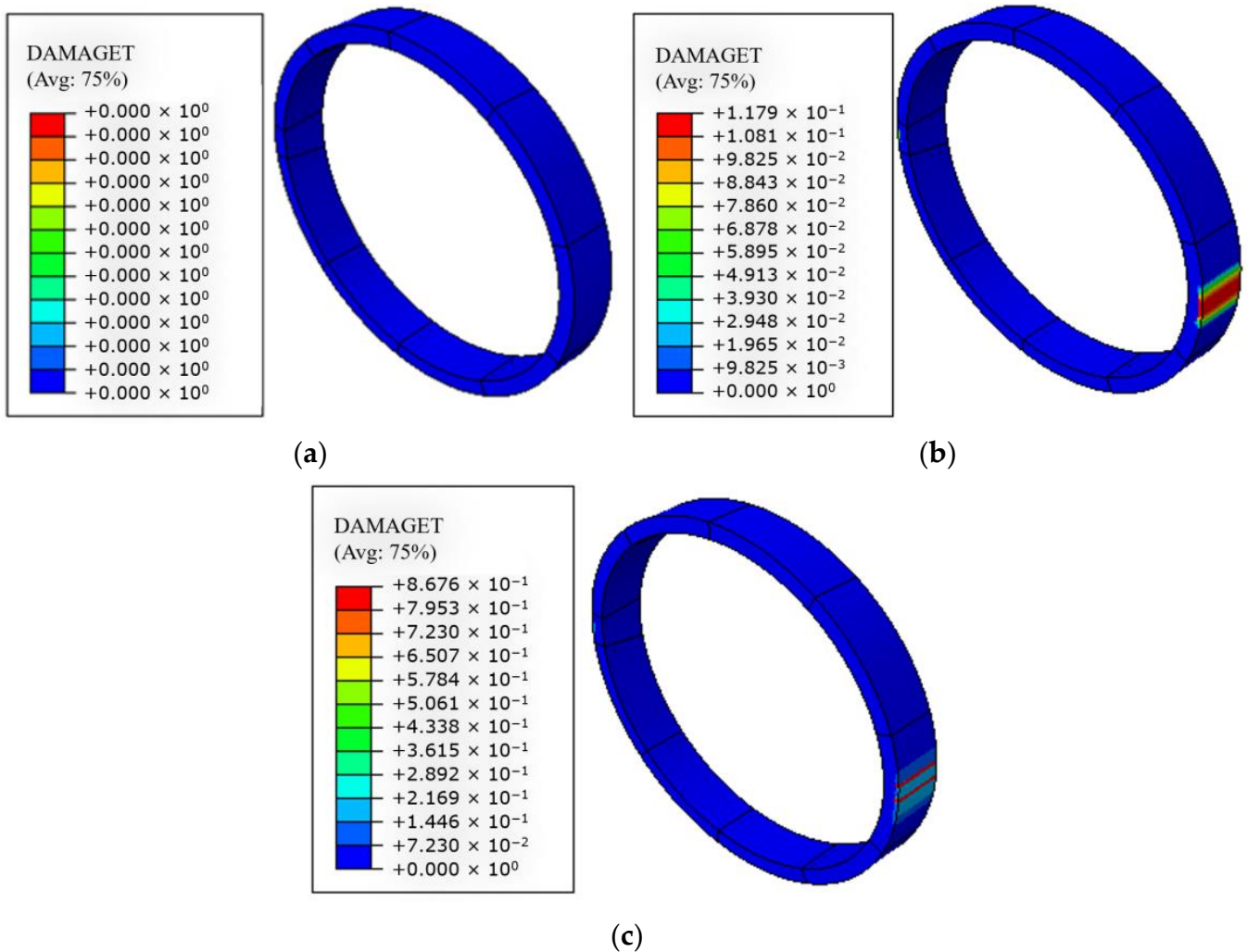


Figure 9. Cloud diagram of tunnel segment tensile damage under different grouting pressure distribution forms: (a) working conditions ①~③; (b) working condition ④; (c) working condition ⑤.

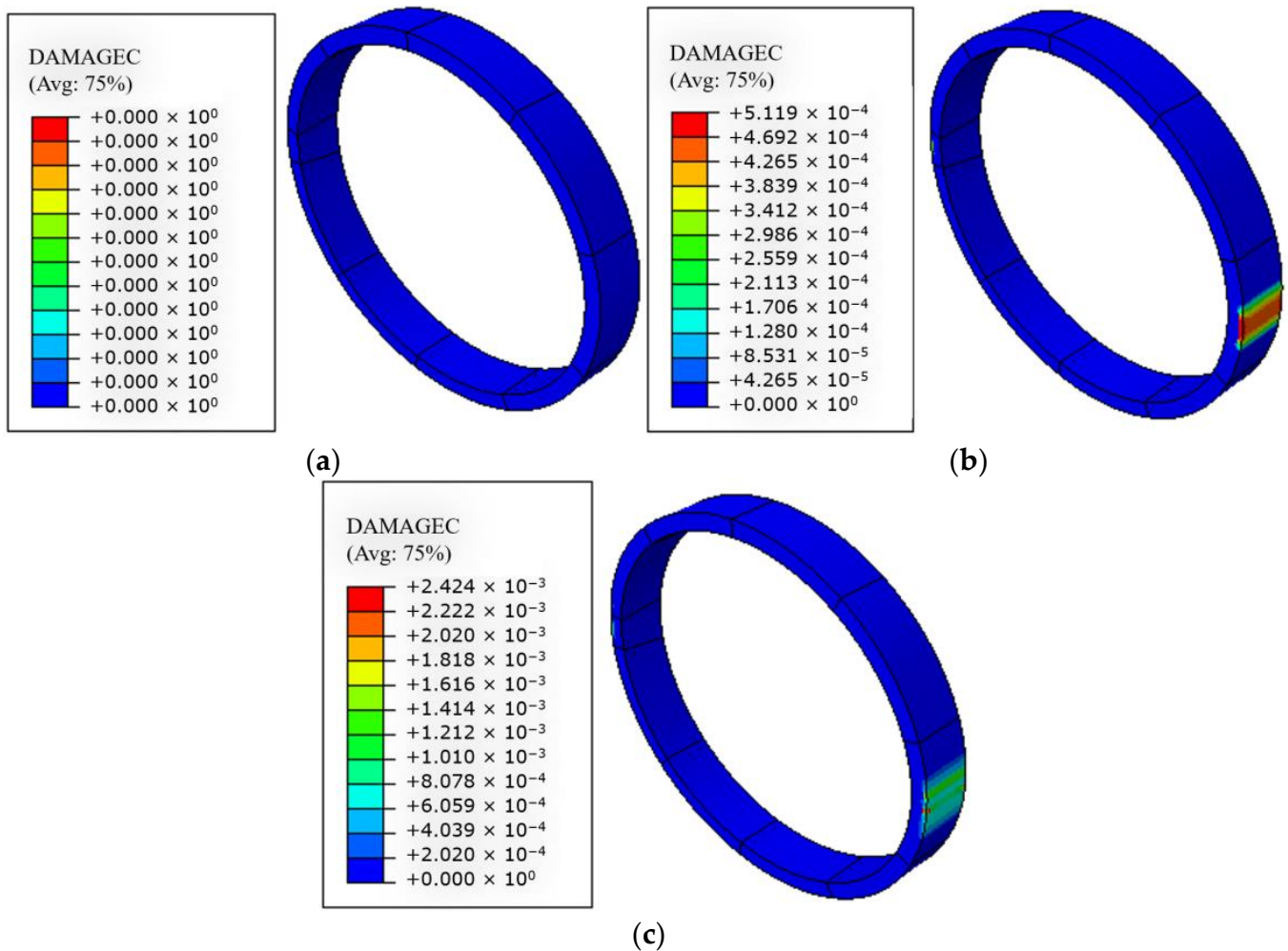


Figure 10. Cloud diagram of tunnel segment pressure damage under different grouting pressure distribution forms: (a) working conditions ①~③; (b) working condition ④; (c) working condition ⑤.

4.2. Internal Force and Stress

Figure 11 shows the bending moment distribution curves of the shield tunnel segment rings for different grouting pressures, and Table 3 lists the bending moments of the tunnel segment rings at the vault, waist, and bottom of the tunnel for the five operating conditions. During homogeneous grouting, the bending moments at different positions of the tunnel segment ring differ by a small amount. As the grout pressure is increased, the bending moment at the vault decreases significantly, while the bending moment at the waist of the arch gradually increases. When the grouting pressure ratio is 2.8, the bending moments of the vault and arch waist are $-1320 \text{ kN}\cdot\text{m}$ and $1760 \text{ kN}\cdot\text{m}$, respectively, and the difference between them reaches $3080 \text{ kN}\cdot\text{m}$. In addition, the absolute value of the maximum bending moment of the whole ring appears at the waist of the arch under the action of the non-uniformly distributed grout pressure. As the grouting pressure ratio gradually increases, the absolute value difference between the arch waist and the arch crown also increases gradually, reaching a maximum of $440 \text{ kN}\cdot\text{m}$. From this, it follows that the distribution of the grouting pressure has a large influence on the internal forces of the segment rings, and that the position of the arch waist is the weak position.

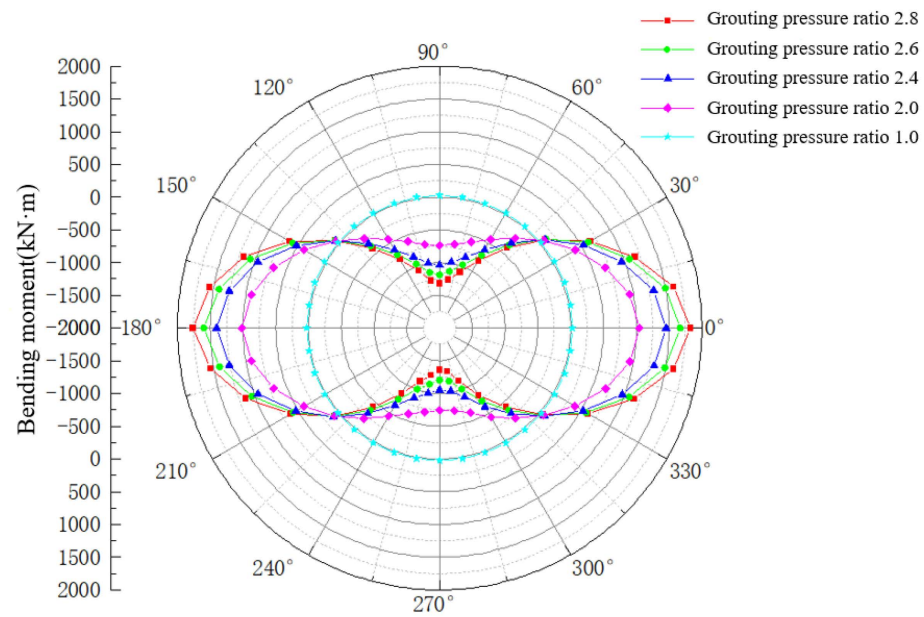


Figure 11. Bending moment distribution of the tunnel segment ring under different grouting pressures.

Table 3. Bending moments at different positions of the segment ring under 5 working conditions.

Working Condition	Grouting Pressure Ratio	Position	Bending Moment/(kN·m)
1	1.0	arch crown (90°)	25.3
		arch waist (180°)	25.9
		arch soffit (270°)	24.5
2	2.0	arch crown (90°)	−739
		arch waist (180°)	1020
		arch soffit (270°)	−742
3	2.4	arch crown (90°)	−1040
		arch waist (180°)	1400
		arch soffit (270°)	−1050
4	2.6	arch crown (90°)	−1190
		arch waist (180°)	1600
		arch soffit (270°)	−1210
5	2.8	arch crown (90°)	−1320
		arch waist (180°)	1760
		arch soffit (270°)	−1360

Figures 12 and 13 show, respectively, the maximum and minimum principal stress cloud diagrams for the shield tunnel segments at a grouting pressure ratio of 2.8 for the pipe rings and bolts. It can be seen from Figure 12 that the outer edge of the waist of the arch and the inner edge of the vault of the segment bear a large main tensile stress. Moreover, the principal tensile stress is greater at the outer edge of the arch waist than at the inner edge of the vault, while the inner edge of the arch waist bears a larger principal compressive stress. The maximum principal tensile stress of the pipe ring is 2.87 MPa, which appears at the outer edge of the arch waist, and the maximum principal compressive stress is 21.99 MPa, which appears at the inner edge of the arch waist. It can be seen from Figure 13 that the maximum principal tensile stress of the bolts in the tunnel segment ring is 337.1 MPa, which is less than the yield strength of 640 MPa, and none of the bolt yields.

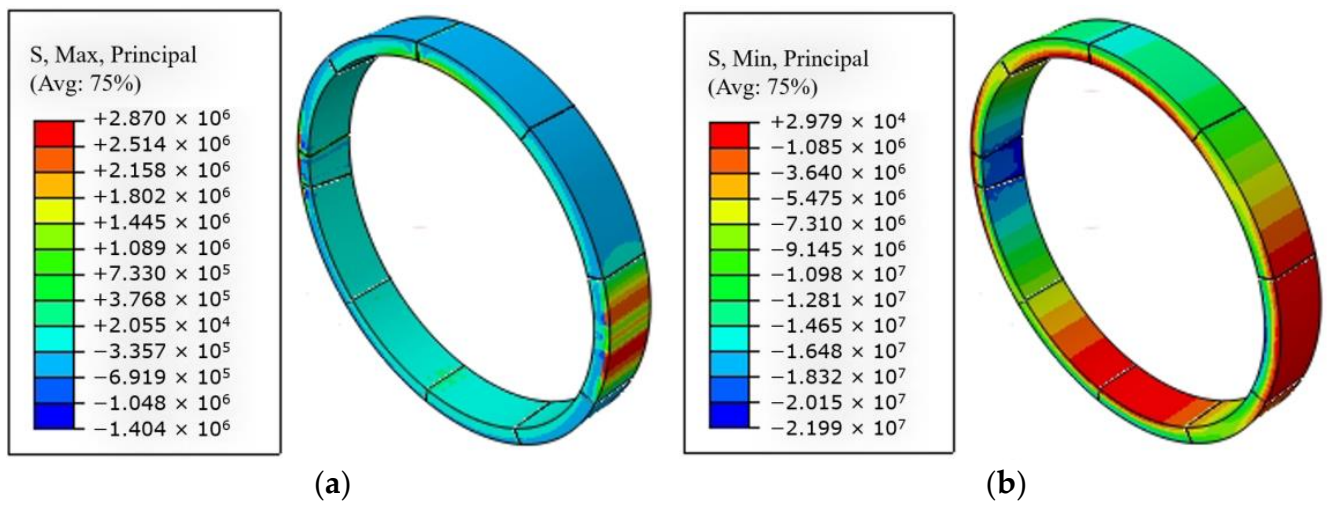


Figure 12. (a) Maximum and (b) minimum principal stress nephograms of tunnel segment rings in working condition ⑤.

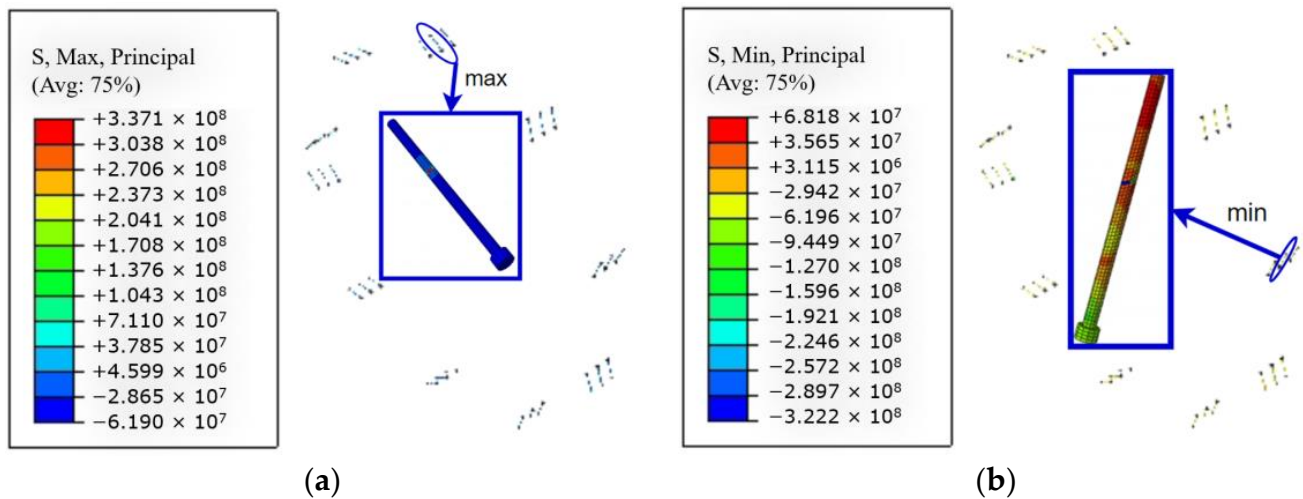


Figure 13. (a) Maximum and (b) minimum principal stress nephograms of tunnel bolts in working condition ⑤.

4.3. Shield Tunnel Deformation

Figure 14 shows the horizontal and vertical displacement contours of the tunnel segment ring at a maximum grouting pressure ratio of 2.8, where the deformation amplification ratio is 20. It can be clearly seen from the figure that the segment ring exhibits a large horizontal displacement outward at the arch waist, while in terms of vertical displacement, the segment ring as a whole is in a floating state, and the floating displacement increases with the increase in the buried depth. At this point, with a grouting pressure ratio of 2.8, the converged deformation of the segment ring waist reaches 39.71 mm and the overall floating value of the tunnel ring reaches 43.12 mm.

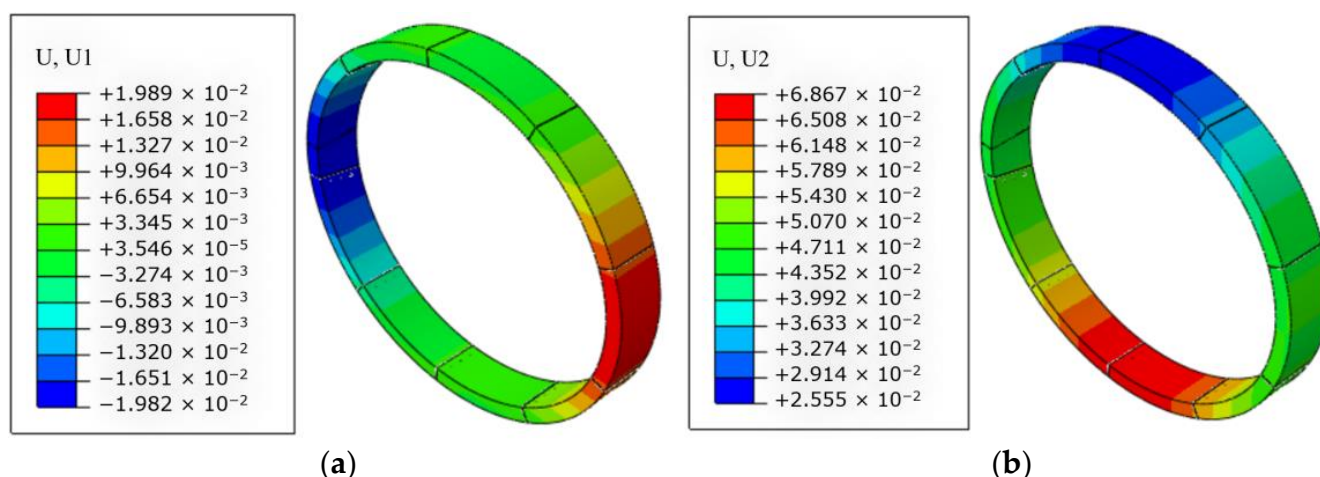


Figure 14. (a) Horizontal and (b) vertical displacement nephograms of segment rings in working condition ⑤.

Table 4 shows the segment ring convergence deformations and the overall floating values for the five different grouting pressure ratios. As can be seen from the table, the distribution of displacements at different positions of the pipe ring is consistent, except for the uniform grouting. And with the increase in the grouting pressure ratio, the convergence deformation and the overall floating value of the waist of the tunnel pipe ring also increase, and the pipe ring as a whole presents a “horizontal duck egg” shape. Combined with Table 3, it can be seen that in the case of uneven grouting, there is a large positive bending moment at the waist of the arch and its transverse displacement value expands outward, which also explains the deformed shape of the pipe ring mentioned above. Second, there is a large negative bending moment at the bottom of the vault, but the grouting pressure at the bottom of the vault is greater than that at the top of the vault, so the overall floating value of the segment ring increases with the increase in the grouting pressure.

Table 4. Segment ring convergence deformation and overall floating value in working condition ⑤.

Grouting Pressure Ratio	Lateral Displacement Value of Left Arch Waist (mm)	Lateral Displacement Value of Right Arch Waist (mm)	Waist Convergence Deformation (mm)	Arch Crown Floating Value (mm)	Arch Bottom Floating Value (mm)	Overall Floating Value of Tunnel Pipe Ring (mm)
1.0	0.99	−0.98	1.97	−5.12	−3.15	1.97
2.0	−1.03	1.03	2.06	12.09	36.59	24.50
2.4	−1.49	1.49	2.98	18.91	52.57	33.66
2.6	−1.73	1.72	3.45	22.28	60.59	38.31
2.8	−1.98	1.99	3.97	25.55	68.67	43.12

The present study conducts a comprehensive numerical simulation analysis on an ultra-large-diameter shield tunnel subjected to asynchronous grouting, serving as a valuable reference for the design and construction of increasingly larger tunnels, including ultra-large-diameter ones. The working conditions adopted in this study are commonly encountered in practical engineering projects, and are specifically based on the Wuhan Lianghu ultra-large-diameter highway tunnel project. To address this issue, most researchers employ numerical methods and field monitoring tests to predict the impact of grouting on tunnel deformation and internal forces. In addition, the presence of joints and cracks in the rock surrounding the tunnel segments may induce variations in grout pressure [29]. An emphasis on analyzing this aspect should be prioritized in future research. Moreover, this study primarily focuses on the overall mechanical and deformation prop-

erties of the tunnel segment, while the localized connection between bolts and segments remains to be explored.

5. Conclusions

In this study, based on the Wuhan Lianghu ultra-large-diameter highway tunnel project, we developed a three-dimensional finite element model using Abaqus, analyzed and discussed the damage evolution, overall floating, converging deformation, and stress of the lining structure during the synchronous grouting process during the construction of a shield tunnel, and can draw the following conclusions:

- (1) The failure mode of a segment under non-uniform synchronous grouting pressure is characterized by tensile failure at the outer edge of the arch waist. Elastic deformation occurs in the segmental concrete of shield tunnels when the grouting pressure ratio between the bottom and top of the vault is less than or equal to 2.4, with increasing tensile damage as this ratio increases. When the grouting pressure ratio is 2.8, the tensile damage to the concrete reaches 0.867.
- (2) The higher the grouting pressure ratio, the greater the positive bending moment value of the segmental arch waist, and the greater the negative bending moment value of both the arch top and bottom. In the case of uneven grouting, a higher principal tensile stress is experienced at the outer edge of the segmental arch waist and inner edge of the vault. Additionally, the outer edge of the arch bears a greater principal tensile stress than the inner edge of the vault, while the inner edge of the arch bears a larger principal compressive stress.
- (3) With the increase in the grouting pressure ratio, the tunnel ring undergoes a distinct “horizontal ellipse” deformation, and there is also a corresponding increase in convergent deformation at the waist of the tunnel pipe ring and overall floating value. At a grouting pressure ratio of 2.8, the converged deformation at the waist measures 39.71 mm, while the overall floating value of the pipe ring reaches 43.12 mm.

Author Contributions: Conceptualization, M.Z.; methodology, M.Z.; software, C.W.; data curation, C.W.; writing—original draft, C.W.; supervision, X.C. and X.B.; funding acquisition, M.S. and X.C. All authors have read and agreed to the published version of the manuscript.

Funding: The research is supported by the National Natural Science Foundation of the People’s Republic of China (52008263).

Data Availability Statement: Not applicable.

Conflicts of Interest: The authors declare no conflict of interest.

References

1. Gan, X.; Yu, J.; Gong, X.; Zhu, M. Characteristics and countermeasures of tunnel heave due to large-diameter shield tunneling underneath. *J. Perform. Constr. Facil.* **2020**, *34*, 04019081. [[CrossRef](#)]
2. Zhang, D.M.; Chen, S.; Wang, R.C.; Zhang, D.M.; Li, B.J. Behaviour of a large-diameter shield tunnel through multi-layered strata. *Tunn. Undergr. Space Technol.* **2021**, *116*, 104062. [[CrossRef](#)]
3. Xie, X.; Yang, Y.; Ji, M. Analysis of ground surface settlement induced by the construction of a large-diameter shield-driven tunnel in Shanghai, China. *Tunn. Undergr. Space Technol.* **2016**, *51*, 120–132. [[CrossRef](#)]
4. Tan, Z.; Li, Z.; Tang, W.; Chen, X.; Duan, J. Research on stress characteristics of segment structure during the construction of the large-diameter shield tunnel and cross-passage. *Symmetry* **2020**, *12*, 1246. [[CrossRef](#)]
5. Avgerinos, V.; Potts, D.M.; Standing, J.R. Numerical investigation of the effects of tunnelling on existing tunnels. *Géotechnique* **2017**, *67*, 808–822. [[CrossRef](#)]
6. Shen, Y.; Zhang, D.; Wang, R.; Li, J.; Huang, Z. SBD-K-medoids-based long-term settlement analysis of shield tunnel. *Transp. Geotech.* **2023**, *42*, 101053. [[CrossRef](#)]
7. Jin, D.; Yuan, D.; Li, X.; Zheng, H. An in-tunnel grouting protection method for excavating twin tunnels beneath an existing tunnel. *Tunn. Undergr. Space Technol.* **2018**, *71*, 27–35. [[CrossRef](#)]
8. Li, P.; Liu, J.; Shi, L.; Zhai, Y.; Huang, D.; Fan, J. A semi-elliptical surface compound diffusion model for synchronous grouting filling stage in specially shaped shield tunnelling. *Int. J. Numer. Anal. Methods Geomech.* **2022**, *46*, 272–296. [[CrossRef](#)]

9. Ye, F.; Yang, T.; Mao, J.; Qin, X.Z.; Zhao, R.L. Half-spherical surface diffusion model of shield tunnel back-fill grouting based on infiltration effect. *Tunn. Undergr. Space Technol.* **2019**, *83*, 274–281. [[CrossRef](#)]
10. Liang, Y.; Huang, X.; Gao, S.; Yin, Y. Study on the Floating of Large Diameter Underwater Shield Tunnel Caused by Synchronous Grouting. *Geofluids* **2022**, *2022*, 2041924. [[CrossRef](#)]
11. Ding, W.; Duan, C.; Zhu, Y.; Zhao, T.; Huang, D.; Li, P. The behavior of synchronous grouting in a quasi-rectangular shield tunnel based on a large visualized model test. *Tunn. Undergr. Space Technol.* **2019**, *83*, 409–424. [[CrossRef](#)]
12. Zou, J.; Zuo, S. Similarity solution for the synchronous grouting of shield tunnel under the vertical non-axisymmetric displacement boundary condition. *Adv. Appl. Math. Mech.* **2017**, *9*, 205–232. [[CrossRef](#)]
13. Bezuijen, A.; Talmon, A.M.; Kaalberg, F.J.; Plugge, R. Field measurements of grout pressures during tunnelling of the Sophia Rail Tunnel. *Soils Found.* **2004**, *44*, 39–48. [[CrossRef](#)]
14. Hashimoto, T.; Brinkman, J.; Konda, T.; Kano, Y.; Feddema, A. Simultaneous backfill grouting, pressure development in construction phase and in the long-term. Tunnelling. *A Decade Prog. GeoDelft* **1995**, *2005*, 101–107.
15. Talmon, A.M.; Bezuijen, A. Simulating the consolidation of TBM grout at Noordplaspolder. *Tunn. Undergr. Space Technol.* **2009**, *24*, 493–499. [[CrossRef](#)]
16. Zhao, T.; Ding, W.; Qiao, Y.; Duan, C. A large-scale synchronous grouting test for a quasi-rectangular shield tunnel: Observation, analysis and interpretation. *Tunn. Undergr. Space Technol.* **2019**, *91*, 103018. [[CrossRef](#)]
17. Lavasan, A.A.; Schanz, T. Numerical investigation of hydromechanical interactions at the tail void of bored tunnels due to grouting. In *Geotechnical Aspects of Underground Construction in Soft Ground*; CRC Press: Boca Raton, FL, USA, 2017; pp. 161–169.
18. Shah, R.; Lavasan, A.A.; Peila, D.; Todaro, C.; Luciani, A.; Schanz, T. Numerical study on backfilling the tail void using a two-component grout. *J. Mater. Civ. Eng.* **2018**, *30*, 04018003.
19. Lavasan, A.A.; Zhao, C.; Barciaga, T.; Schaufler, A.; Steeb, H.; Schanz, T. Numerical investigation of tunneling in saturated soil: The role of construction and operation periods. *Acta Geotech.* **2018**, *13*, 671–691.
20. Lou, P.; Li, Y.; Lu, S.; Xiao, H.; Zhang, Z. Deformation and Mechanical Characteristics of Existing Foundation Pit and Tunnel Itself Caused by Shield Tunnel Undercrossing. *Symmetry* **2022**, *14*, 263. [[CrossRef](#)]
21. Liang, Y.; Zhang, J.; Lai, Z.S.; Huang, Q.Y.; Huang, L.C. Temporal and spatial distribution of the grout pressure and its effects on lining segments during synchronous grouting in shield tunnelling. *Eur. J. Environ. Civ. Eng.* **2020**, *24*, 79–96. [[CrossRef](#)]
22. Gan, X.; Yu, J.; Gong, X.; Hou, Y.; Liu, N.; Zhu, M. Response of operating metro tunnels to compensation grouting of an underlying large-diameter shield tunnel: A case study in Hangzhou. *Undergr. Space* **2022**, *7*, 219–232.
23. *GB 50010-2010*; Code for Design of Concrete Structures. China Standard Press: Beijing, China, 2010.
24. Su, D.; Chen, W.; Wang, X.; Huang, M.; Pang, X.; Chen, X. Numerical study on transverse deformation characteristics of shield tunnel subject to local soil loosening. *Undergr. Space* **2022**, *7*, 106–121.
25. Koyama, Y. Present status and technology of shield tunneling method in Japan. *Tunn. Undergr. Space Technol.* **2003**, *18*, 145–159.
26. Wang, F.; Zhang, D.M.; Zhu, H.H.; Huang, H.W.; Yin, J.H. Impact of overhead excavation on an existing shield tunnel: Field monitoring and a full 3D finite element analysis. *Comput. Mater. Contin.* **2013**, *34*, 63–81.
27. Zhou, L.; Zhu, H.H.; Shen, Y.; Yan, Z.; Guan, L. Stress and deformation properties of shield segmental linings under internal water pressures. *Chin. J. Geotech. Eng.* **2023**, *45*, 1763–1772. (In Chinese)
28. Fu, Y.B.; Zhao, J.; Wu, X.; Zhong, J.Y. Back-fill pressure model research of simultaneous grouting for shield tunnel. *J. Disaster Prev. Mitig. Eng.* **2016**, *36*, 107–113. (In Chinese)
29. Shahsavari, J.; Johari, A.; Binesh, S. Stochastic analysis of rock slope stability considering cracked rock masses. In Proceedings of the International Conference on Civil Engineering: Modern and Practical Findings, Shiraz, Iran, 15 December 2021.

Disclaimer/Publisher’s Note: The statements, opinions and data contained in all publications are solely those of the individual author(s) and contributor(s) and not of MDPI and/or the editor(s). MDPI and/or the editor(s) disclaim responsibility for any injury to people or property resulting from any ideas, methods, instructions or products referred to in the content.